AGU PUBLICATIONS

JGR

Journal of Geophysical Research: Solid Earth

RESEARCH ARTICLE

10.1002/2016JB013834

Key Points:
- A strongly magnetic zone was observed in a red soil developed on basalt with chi up to 10×10^{-5} m^3 kg^{-1} in northern Hainan Island, China
- The strongly magnetic zone contains a significant amount of superparamagnetic particles that originated mainly from volcanic ash
- The layer above the strongly magnetic zone experienced a warmer and more humid climate than the layer below

Correspondence to:
G. Wei and Q. Liu,
gjwei@mail.gig.ac.cn;
qsliu@sustc.edu.cn

Citation:
Liu, Z., J. Ma, G. Wei, Q. Liu, Z. Jiang, X. Ding, S. Peng, T. Zeng, and T. Ouyang (2017), Magnetism of a red soil core derived from basalt, northern Hainan Island, China: Volcanic ash versus pedogenesis, *J. Geophys. Res. Solid Earth*, *122*, 1677–1696, doi:10.1002/2016JB013834.

Received 6 DEC 2016
Accepted 4 MAR 2017
Accepted article online 7 MAR 2017
Published online 30 MAR 2017

Magnetism of a red soil core derived from basalt, northern Hainan Island, China: Volcanic ash versus pedogenesis

Zhifeng Liu[1,2], Jinlong Ma[1], Gangjian Wei[1], Qingsong Liu[3,4], Zhaoxia Jiang[5], Xing Ding[1], Shasha Peng[2], Ti Zeng[2], and Tingping Ouyang[2]

[1]State Key Laboratory of Isotope Geochemistry, Guangzhou Institute of Geochemistry, Chinese Academy of Sciences, Guangzhou, China, [2]Key Laboratory of Ocean and Marginal Sea Geology, Guangzhou Institute of Geochemistry, Chinese Academy of Sciences, Guangzhou, China, [3]Department of Marine Science and Engineering, Southern University of Science and Technology of China, Shenzhen, China, [4]Lababoratory for Marine Geology, Qingdao National Oceanography Laboratory for Science and Technology, Qingdao, China, [5]State Key Laboratory of Lithospheric Evolution, Institute of Geology and Geophysics, Chinese Academy of Sciences, Beijing, China

Abstract Similar to loess-paleosol sequences in northwestern China, terrestrial sedimentary sequences (red soils) in southern China also provide sensitive Quaternary records of subtropical/tropical paleoclimate and paleoenvironment. Compared with red clay sequences originated from eolian dust, red soils derived from bedrock have received little attention. In this study, a long core of red soil derived from weathered basalt in northern Hainan Island, China, was systematically investigated by using detailed magnetic measurements and rare earth element analyses. The results show that an extremely strong magnetic zone with a maximum magnetic susceptibility ($>10 \times 10^{-5}$ m^3 kg^{-1}) is interbedded in the middle of the core profile. This layer contains a significant amount of superparamagnetic magnetite/maghemite particles that primarily originated from volcanic ash, with secondary contributions from pedogenesis. The former has an average grain size of ~19 nm with a normal distribution of volume, and the latter has a much wider grain size distribution. The presence of volcanic ash within the red soil indicates that these Quaternary basalts were not formed by continuous volcanic eruptions. Moreover, the magnetic enhancement patterns differ between the upper and lower zones. The upper zone is more magnetically enhanced and experienced higher precipitation and temperature than the lower zone. Discrimination of superparamagnetic particles originating from pedogenic processes and volcanic ash thus provides a sound theoretical base for accurate interpretation of magnetism in red soils in this region.

1. Introduction

The interbedded loess/paleosol sequences on the Chinese Loess Plateau (CLP) contain a magnetic record of Quaternary paleoclimate and, in particular, of the evolution of the East Asia Summer/Winter Monsoon (EASM), as well as paleoprecipitation [*Liu et al.*, 2007; *Liu and Ding*, 1998; *Maher and Thompson*, 1999; *Maher et al.*, 1994]. Under aerobic conditions, the magnetism of topsoils is generally enhanced due to the in situ pedogenic formation of secondary ultrafine ferrimagnetic minerals [*Maher and Taylor*, 1988; *Zhou et al.*, 1990], which is directly related to climatic conditions and, especially, precipitation [*Balsam et al.*, 2011; *Florindo et al.*, 1999a, 1999b; *Han et al.*, 1996; *Hyland et al.*, 2015; *Jordanova et al.*, 2016; *Liu et al.*, 1995; *Maher*, 1998; *Maher and Thompson*, 1995; *Maher et al.*, 1994].

In addition to the loess/paleosol sequences on the CLP in northwestern China, red soils that contain abundant hematite (Hm) are widespread in tropical regions of China (south and east of the Yangtze River and Tibetan Plateau, respectively), covering an area of ~2×10^6 km^2 [*Huang et al.*, 1996; *C. Liu et al.*, 2010]. These red soils are formerly known as Laterites and are now classed as Ferralsols and Plinthosols (World Reference Base for Soil Resources) or oxisols (U.S. Department of Agriculture Soil Taxonomy) [*Chesworth*, 2008].The red soil sequences also provide sensitive Quaternary records of paleoclimate and paleoenvironment in these regions [*C. Liu et al.*, 2012; *Zhang et al.*, 2007, 2009]. The parent materials for these reddish sequences are eolian dust, bedrock, or other residual materials. Soils are formed by the weathering of these parent materials, and their physical and chemical properties are controlled by various factors, including the texture and structure of the parent material, climate, organisms, topography, and time [*Jenny*, 1941].

Climate has a large influence on the physical and chemical properties of red soils. In cold and dry regions, only rock debris can be formed. For example, *Chevrier et al.* [2006] reported that only a ~3 cm thick layer of Jurassic basalt was altered by neoformation of maghemite (Mgh) and (oxy)hydroxides during slow weathering in the cold and arid climate of Antarctica. However, the depth of soil developed on basalt can reach several meters in subtropical regions [*Brimhall et al.*, 1991; *Eggleton et al.*, 1987; *Su et al.*, 2015]. In tropical regions, red soils can even reach depths of >20 m due to extreme weathering and the warm-humid climate [*Huang et al.*, 1996; *Ma et al.*, 2007] and thus have the potential to record high-resolution paleoclimatic signals.

Pedogenic ferrimagnetic minerals accumulate from a minimum mean annual precipitation (MAP) of ~200 mm/yr to a maximum MAP of ~1200 mm/yr and are then gradually dissolved or altered as the MAP increases and, finally, cease accumulation at a MAP of ~2200 mm/yr [*Balsam et al.*, 2011]. In tropical regions, precipitation is higher than the threshold (~1200 mm/yr), and fine magnetic minerals are easily altered, meaning the origins and transformations of magnetic minerals become complicated. For example, *Maher and Thompson* [1995] argued that pedogenic susceptibility of soil peaks at a MAP of ~1200 mm/yr and then decreases above that due to the transformation of strong ferrimagnetic to weak antiferromagnetic minerals. Subsequently, *Han et al.* [1996] documented that the χ values of topsoil rise with increasing MAP and mean annual temperature (MAT) in temperate and semiarid regions, whereas they decrease with increasing MAP and MAT in subtropical and tropical regions. Recently, *Long et al.* [2011] investigated a set of Ferralsols derived from basalt with MAP from 1440 to 2020 mm/yr and MAT of ~24°C in northern Hainan Island and found that χ negatively correlates with MAP.

In tropical regions, the balance between mineral production and dissolution determines the end-product nature of pedogenic minerals. Given that the red soil derived from parent rocks in tropical regions can reach a depth of >20 m, the magnetic properties of such soil change dramatically with depth. For example, *Van Dam et al.* [2008] documented that magnetic properties of basaltic substrate soils in tropical Hawaii generally increase with increasing soil development. However, *Ouyang et al.* [2015] studied a 4.5 m long weathered basalt section from a location with a MAP of ~1500 mm/yr and suggested that the coarse (pseudo-single domain; PSD) magnetic particles in the parent basalt were transformed into SD particles in the middle of the section and superparamagnetic (SP) and SD particles in the upper part. Although fine magnetic particles were formed, the topsoil had a lower χ than the parent basalt. Recently, *Long et al.* [2015] investigated the magnetic properties of three red Ferralsols from localities with MAP from 1440 to 1650 mm/yr and noted that χ is generally 3–20 times higher than that of unweathered basalt and ferrimagnetic material becomes enriched as the hematite (Hm) content increases in the profile. Due to soil drainage and leaching processes, magnetic properties differ greatly among these red soils, despite their similar parent material. As such, magnetic investigations of tropical soils can further our understanding of the origin and transformation of magnetic minerals in humid-warm conditions.

In this study, detailed magnetic and rare earth element (REE) analysis was conducted on a strong magnetic zone and its adjacent lower and upper zones from a long core of red soil (~50 m, and the top is Ferralsol) developed on basalt from northern Hainan Island, China. The objectives of this study were to (1) characterize the magnetic mineralogy of the highly magnetic zone and its two adjacent zones, (2) understand the mechanisms of magnetic enhancement in these three different zones and the mineral transformations during pedogenesis under extreme weathering, and (3) reconstruct the paleoenvironmental conditions during red soil formation.

2. Materials and Methods

2.1. Site and Samples

Hainan is separated by the Qiongzhou Strait from Leizhou Peninsula of Guangdong Province and is the second largest island in China. Given the high topography in central Hainan, most of its rivers originate in the central area and flow radially in various directions (Figure 1). The Chengmai (CM) profile (19.77°N, 110°E) is located ~4 km north of Chengmai County and ~35 km southwest of Haikou, which is the capital of Hainan Province. The climate of CM is tropical with high temperature and precipitation. The MAP is 1760 mm/yr and MAT is 23.7°C, with evaporation of 1830 mm/yr (mean value from 1959 to 2008 and data is from China Meteorological Administration). The topography of sampling site is horizontal. Due to the EASM, ~80% of annual precipitation occurs from May to October.

Figure 1. Location map showing the sampling site on Hainan Island; CM is the study site.

All samples were obtained from a 55 m long core of weathered basalt at intervals of 10 cm. The collected samples were dried at 40°C, gently crushed, homogenized, wrapped in polycarbonate preservative film, and packed into weakly diamagnetic, cubic, plastic sample holders (8 cm^3) for further magnetic measurements.

2.2. Methods

Low-field mass-specific magnetic susceptibility (χ) measurements were conducted by using a multifunction kappabridge (MFK-FA) at three operating frequencies (976, 3904, and 15,616 Hz) in a magnetic field of 200 Am^{-1}. χ_{FD} was used as a proxy for the presence of ultrafine-grained (<0.01 μm) magnetic minerals and defined as $\chi_{FD} = \chi_{LF} - \chi_{HF}$ [*Dearing et al.*, 1996b] (χ_{LF} and χ_{HF} are the susceptibility measured at low and high frequencies, respectively). In this study, the low and high frequencies applied to the χ measurements were 976 and 15,616 Hz, respectively. χ_{FD}% defined as $\chi_{FD}\% = (\chi_{LF} - \chi_{HF})/\chi_{LF} \times 100\%$ is controlled by both the grain size distribution (GSD) of SP and SD particles and by the relative concentrations of SP, SD, and PSD particles [*Eyre*, 1997; *Liu et al.*, 2005a; *Worm*, 1998].

Anhysteretic remanent magnetization (ARM) is sensitive to SD particles [*Banerjee et al.*, 1981; *King et al.*, 1982] and was obtained with a D-2000 alternating demagnetizer with an alternating field of 100 mT and a superimposed bias field of 0.05 mT. Saturation isothermal remanent magnetization (SIRM) was produced with an IM-10-30 pulse magnetizer at a magnetic field of 1 T. Both ARM and SIRM were measured with an AGICO JR-6A spinner magnetometer. The ARM/SIRM ratio can be used to reveal the grain size of magnetic particles without the influence of SP particles, and a low ratio indicates a small grain size [*Q. Liu et al.*, 2012]. After measurement of SIRM, a 0.3 T backfield was imposed to acquire the S-ratio and HIRM. The S-ratio (S-ratio = $IRM_{-0.3\,T}$/SIRM) was used to estimate the relative content of ferrimagnets (e.g., magnetite; Mgt) versus antiferromagnets (e.g., Hm). The HIRM (HIRM = $0.5 \times (SIRM + IRM_{-0.3\,T})$) is an indicator of the absolute content of antiferromagnets.

Room temperature hysteresis loops, IRM, backfield demagnetization, and first-order reversal curves (FORCs) were measured by using a Princeton Vibrating Sample Magnetometer (MicroMag 3900). The saturation field was 1 T with a field step of 5 mT and an averaging time of 200 ms. Hysteresis parameters such as coercivity (B_c), remanence magnetization (M_{rs}), and saturation magnetization (M_s) were calculated after subtracting the high-field paramagnetic contributions. Remanence coercivity (B_{cr}) was obtained from the backfield demagnetization curves. The IRM acquisition curves were measured by using the logarithmic sweep mode with an initial field of 1 mT and a total of 80 measurement points. IRM curves of selected samples were unmixed into different coercivity components through cumulative log-Gaussian analysis [*Heslop et al.*, 2002; *Kruiver et al.*, 2001; *Robertson and France*, 1994]. FORC data [*Pike et al.*, 1999; *Roberts et al.*, 2000; *Roberts et al.*, 2014] were measured with a maximum field of 1 T and averaging time of 200 ms. A total of

120–200 partial hysteresis loops were measured. FORC diagrams were processed by using Forcinel v1.18 with a smoothing factor (SF) between 3 and 5 [*Harrison and Feinberg*, 2008].

The high-temperature dependent susceptibility curve (χ-*T*) is sensitive to subtle changes in magnetic minerals during thermal treatments and has been used as a routine rock magnetic tool to identify the magnetic mineralogy through Curie temperatures [*Evans and Heller*, 2003]. χ-*T* measurements were conducted by using an MFK-FA coupled with a high-temperature attachment. The temperature was cycled from room temperature to 700°C.

Low-temperature measurements were conducted by using a Quantum Design magnetic property measurement system (MPMS XL-5) in the Paleomagnetism and Chronology Laboratory, Institute of Geology and Geophysics, Chinese Academy of Sciences, Beijing, China. Zero-field cooling (ZFC) and field cooling (FC) curves were measured between 10 and 300 K, with a sweep rate of 5 K/min. Samples were cooled to 10 K in a zero field (ZFC measurements) or a 2.5 T (FC measurements) field first, and then a 2.5 T field was applied to obtain a low-temperature SIRM. After the field was switched off, the warming SIRM measurements were performed from 10 to 300 K at a zero field. ZFC measurements were carried out before FC measurements. Alternating current (AC) magnetic susceptibility was measured between 5 and 300 K at 5 K intervals at frequencies of 1, 10, and 100 Hz, and the temperature dependence of χ_{FD} was calculated as the difference of $\chi_{1Hz} - \chi_{10Hz}$ and $\chi_{1Hz} - \chi_{100Hz}$. The temperature dependence of χ_{FD} was first used to estimate the size distribution of pedogenic magnetic particles by *Liu et al.* [2005a], and the corresponding temperature with maximum χ_{FD} can be interpreted as the average grain size.

For trace element analysis, the selected bulk samples were crushed to power and then dried at 105°C to remove absorbed water. The dried samples were baked at 700°C for 4 h to remove organic material and then digested in a mixed solution of nitric acid + hydrofluoric acid. Trace elements were measured by using a Perkin-Elmer Elan 6000 inductively coupled plasma–mass spectrometer with a detection limit of ~10 ppb and errors of less than 5%, at Guangzhou Institute of Geochemistry, Chinese Academy of Sciences (GIGCAS), Guangzhou, China. In this study, the REE concentrations were normalized to post-Archean Australian shale (PAAS) [*Nance and Taylor*, 1976].

3. Results

3.1. Variations in Rock Magnetic Parameters With Depth

The studied red soil core can be divided into an upper zone (UZ; 20.0–22.0 m), a strongly magnetic zone (SMZ; 22.0–23.8 m), and a lower zone (LZ; 23.8–25.9 m) (Figure 2 and Table 1). χ is routinely used to indicate the concentration of ferrimagnetic minerals in environmental samples [*Dearing et al.*, 1996b; *Thompson and Oldfield*, 1986]. In this study, the parent material (CM-44.7) is less weathered and contains a few fine magnetic particles with χ of $104.3 \times 10^{-8}\,m^3\,kg^{-1}$ and χ_{FD}% of only 2.5% (Figure 2 and Table 1). χ changes dramatically with depth from ~500–$2300 \times 10^{-8}\,m^3\,kg^{-1}$ in the UZ, to more than $10{,}000 \times 10^{-8}\,m^3\,kg^{-1}$ at 23.0 m (CM-23.0) in the SMZ (Figure 2b) and to ~200–$900 \times 10^{-8}\,m^3\,kg^{-1}$ in the LZ. The χ of CM-23.0 is about 36 times higher than the maximum χ of Luochuan loess (located in the fifth paleosol sequence, and the maximum value is $275 \times 10^{-8}\,m^3\,kg^{-1}$), which is one of the highest susceptibility measurements of natural soil. Possible explanations for the extremely high χ from 22.0 to 23.8 m (shaded zone in Figure 2b) include the presence of biogenic fine-grained Mgt, volcanic tephra, and pedogenesis. The rock magnetic parameters from 20.0 to 25.9 m were investigated in detail to better understand the magnetic mineralogy in the SMZ (Figures 2b–2i).

χ_{FD} is an indicator of fine magnetic particles near the SP/SD threshold [*Dearing et al.*, 1996b; *Q. Liu et al.*, 2012; *Worm*, 1998] and displays similar variations to χ. χ_{FD} is up to ~$1200 \times 10^{-8}\,m^3\,kg^{-1}$ in the SMZ, and the average χ_{FD} in the SMZ is about 3 and 18 times higher than that in the UZ and LZ, respectively (Figure 2c). χ_{FD}% generally decreases with increasing depth, ranging between ~5% and 23%. In the UZ, χ_{FD}% is elevated in its middle section, changing from ~12% to 23%. In the SMZ, χ_{FD}% decreases downward from ~16% to 5%, with a mean value of 10.4% (Figure 2d). In the LZ, χ_{FD}% is relatively low and constant (7.8% ± 1%) (Table 1). χ_{FD}% is controlled by both GSD and the concentration of particles near the SP/SD threshold (~20–25 nm) [*Eyre*, 1997; *Liu et al.*, 2005a; *Worm*, 1998]. Low χ_{FD}% (<15%) is attributed to low concentrations of SP particles, broad GSD, or a bimodal GSD [*Worm*, 1998].

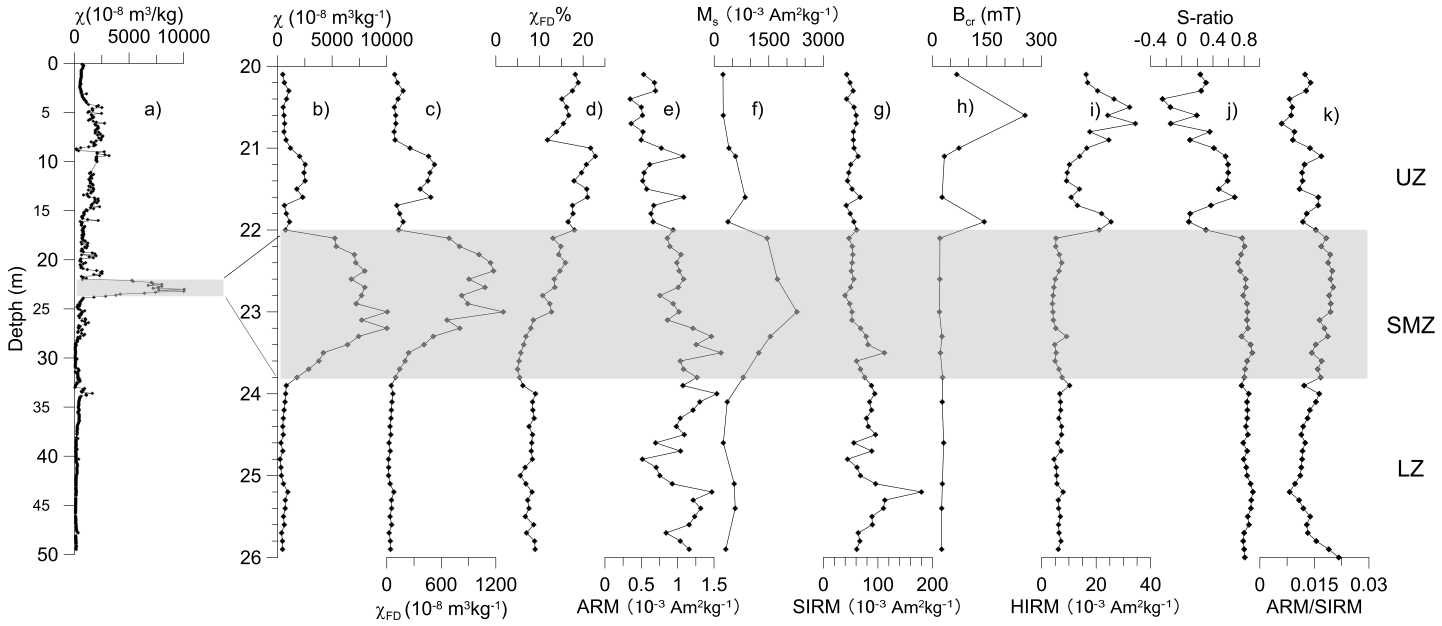

Figure 2. Variations in magnetic parameters with depth. The studied red soil is divided into an upper zone (UZ; 20.0–22.0 m), a strongly magnetic zone (SMZ; 22.0–23.8 m), and a lower zone (LZ; 23.8–25.9 m).

ARM is sensitive to SD particles [*Evans and Heller*, 2003] and generally increases down-core (Figure 2e). M_s is independent of grain size and is an excellent indicator of the concentration of magnetic minerals [*Q. Liu et al.*, 2012; *Thompson and Oldfield*, 1986]. M_s values are remarkably high in the SMZ due to the abundance of magnetic minerals (Figure 2g). SIRM, which is used to estimate the concentration of large magnetic particles (SD, PSD, and MD), is relatively constant throughout the core, apart from the high value at ~25.2 m. This high SIRM value is due to the presence of SD particles, as ARM also shows a high value at ~25.2 m. The relatively high values of ARM/SIRM in the SMZ indicate the small grain size of the magnetic minerals above the SP/SD threshold (Figure 2k).

HIRM, which is a semiquantitative proxy for Hm content, displays relatively low values below depths of 22.1 m (SMZ and LZ), but high values in the UZ, particularly in the intervals 20.2–21.2 and 21.6–22.0 m (Figure 2i). The S-ratio of the parent material (0.94) is higher than that of the studied core (0.64) (Table 1), suggesting that the relative concentration of antiferromagnetic minerals increased during pedogenesis. The S-ratio values are relatively constant in the SMZ (0.81) and LZ (0.84), indicating the dominance of ferrimagnets and a considerable amount of Hm [*Thompson and Oldfield*, 1986]. In the UZ, the S-ratio values vary from −0.25 to 0.68, reflecting high concentrations of Hm, which is also consistent with the high HIRM and B_{cr} in this zone (Figures 2g, 2i, and 2j).

3.2. IRM Acquisition Curves and Unmixing Components

IRM acquisition curves and coercivity component unmixing results for typical samples are displayed in Figure 3, which shows three different patterns. The curves in the SMZ (CM-22.6, CM-23.0, and CM-23.5) get ~90% of the SIRM when the applied field is 0.1 T and almost ~97% at 0.3 T (Figures 3b1, 3c1, and 3d1). This behavior indicates the dominance of "soft" magnetic minerals. For the parent material (CM-44.7), the IRM curve gets ~60% of SIRM at 0.1 T and ~97% at 0.3 T (Figure 3f1). IRM curves for samples CM-21.1 and CM-24.6 exhibit similar behavior, reaching 80% and 90% of SIRM at 0.3 T, respectively, and then generally increase from 0.3 to 1 T, suggesting a dominance of both "hard" and "soft" magnetic minerals (Figures 3a1 and 3e1).

IRM acquisition curves can be decomposed into curves for individual magnetic minerals with the half saturated field ($B_{1/2}$) and dispersion parameter (DP), based on cumulative log-Gaussian (CLG) analysis [*Heslop et al.*, 2002; *Kruiver et al.*, 2001; *Robertson and France*, 1994]. Detailed unmixing results for the IRM acquisition curves of typical samples are shown in Table 2 and Figure 3. IRM curves for samples from the

Journal of Geophysical Research: Solid Earth
10.1002/2016JB013834

Table 1. Statistics of the Magnetic Parameters in UZ, SMZ, and LZ[a]

		χ (10^{-8} m^3 kg^{-1})	χ_{FD} (10^{-8} m^3 kg^{-1})	χ_{FD}%	ARM (10^{-3} Am^2 kg^{-1})	SIRM (10^{-3} Am^2 kg^{-1})	S-ratio	HIRM (10^{-3} Am^2 kg^{-1})	B_{cr} (mT)	B_c (mT)	M_{rs} (10^{-3} Am^2 kg^{-1})	M_s (10^{-3} Am^2 kg^{-1})
UZ	*N*	20	20	20	20	20	20	20	6	6	6	6
	Mean	1,202.20	227.37	17.92	0.64	53.21	0.28	18.94	99.84	8.33	74.89	451.03
	Min	479.04	81.33	11.83	0.35	41.91	−0.25	9.12	26.95	3.95	54.22	240.51
	Max	2,531.01	525.04	22.80	1.08	67.43	0.68	34.39	255.30	16.95	95.92	849.78
	SD	750.14	164.16	2.73	0.20	7.33	0.27	7.35	86.64	4.75	13.45	232.36
SMZ	*N*	18	18	18	18	18	18	18	6	6	6	6
	Mean	6,483.25	714.86	10.40	1.08	61.14	0.81	5.55	23.07	2.37	74.12	1,504.50
	Min	1,777.40	96.90	4.97	0.76	39.66	0.72	3.94	19.53	0.76	51.44	796.16
	Max	10,050.45	1,281.90	15.94	1.60	111.83	0.91	9.15	28.36	5.23	135.92	2,273.55
	SD	2,244.51	373.35	3.91	0.21	17.19	0.05	1.39	3.57	1.91	32.00	495.81
LZ	*N*	21	21	21	21	21	21	21	5	5	5	5
	Mean	538.87	42.38	7.83	1.06	85.70	0.84	6.60	27.63	12.47	94.32	410.16
	Min	227.12	19.04	5.62	0.51	44.32	0.77	4.57	25.83	10.78	65.69	249.78
	Max	936.65	77.75	9.10	1.54	179.79	0.91	10.26	31.37	14.96	128.06	576.41
	SD	179.72	15.47	0.99	0.26	27.82	0.04	1.14	2.26	1.63	29.34	145.04
Sum	*N*	59	59	59	59	59	59	59	17	17	17	17
	Mean	2,577.26	310.25	12.03	0.92	67.19	0.64	10.46	51.51	7.44	80.33	810.82
	Min	227.12	19.04	4.97	0.35	39.66	−0.25	3.94	19.53	0.76	51.44	240.51
	Max	10,050.45	1,281.90	22.80	1.60	179.79	0.91	34.39	255.30	16.95	135.92	2,273.55
	SD	2,926.32	359.06	5.14	0.30	23.96	0.30	7.51	60.89	5.17	26.04	614.91
Parent		104.30	2.51	2.41	0.30	46.92	0.94	2.73	60.00	28.93	47.16	155.60

[a]*N*: number of samples, SD: standard deviation, parent: CM-44.7

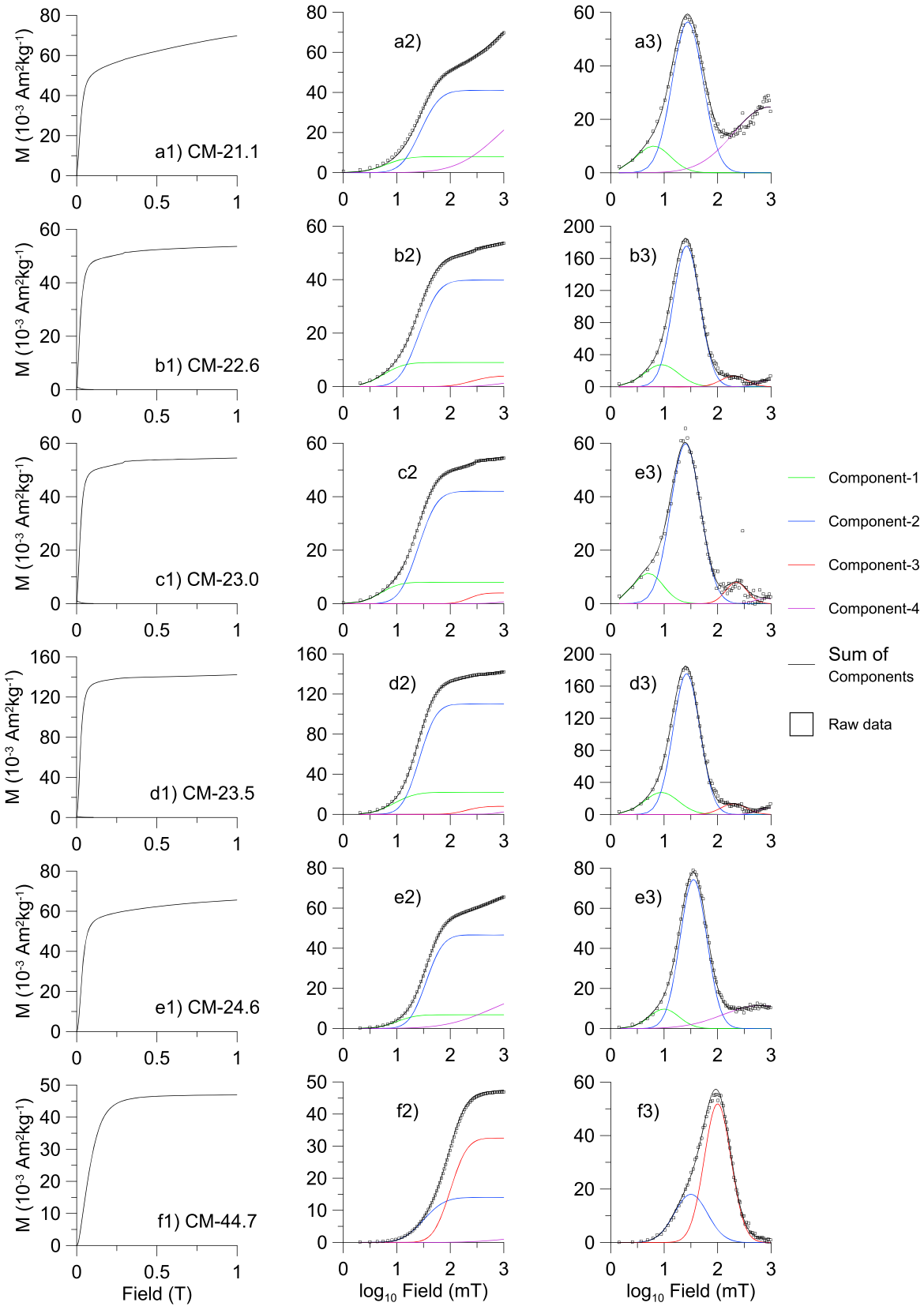

Figure 3. Isothermal remanent magnetization (IRM) curves and their unmixed CLG components for typical samples. The term CM-21.1, as an example, denotes that the sample was collected between 21.0 and 21.1 m depth.

Table 2. Detailed Unmixing Results of IRM Acquisition Curves for Typical Samples[a]

		CM-21.1	CM-22.6	CM-23.0	CM-23.5	CM-24.6	CM-44.7
SIRM (10^{-3} Am^2 kg^{-1})		67.75	53.6	54.47	142.23	65.58	46.92
Component 1	$B_{1/2}$ (mT)	6.3	5.6	5.0	8.9	10.0	
	%SIRM	9.0	16.4	14.5	15.3	9.3	
	DP	0.31	0.31	0.28	0.35	0.28	
Component 2	$B_{1/2}$ (mT)	27.5	26.3	25.1	26.3	35.5	31.6
	%SIRM	46.1	72.6	76.4	76.4	63.5	29.2
	DP	0.29	0.29	0.28	0.25	0.25	0.31
Component 3	$B_{1/2}$ (mT)		251.2	223.9	177.8		100.0
	%SIRM		7.3	7.3	5.6		69.7
	DP		0.30	0.20	0.24		0.26
Component 4	$B_{1/2}$ (mT)	891.3	794.3	891.3	891.3	631.0	707.9
	%SIRM	44.9	3.6	1.8	2.8	27.2	3.1
	DP	0.65	0.32	0.20	0.20	0.69	0.4

[a] $B_{1/2}$ is the field for the component to acquire half SIRM; %SIRM is the contribution of the component to the total SIRM; DP is the dispersion parameter, describing the coercivity distribution of the component.

SMZ (CM-22.6, CM-23.0, and CM-23.5) unmixed into four components: (1) very low coercivity (5–10 mT) component 1, (2) low coercivity (25–36 mT) component 2, (3) medium coercivity component 3 (178–251 mT), and (4) high coercivity (631–891 mT) component 4. Samples from the UZ (CM-21.1) and LZ (CM-24.6) have three of these components but lack component 3 (Table 2 and Figure 3). The parent material (CM-44.7) is unmixed into three components but did not contain the very low coercivity component 1 (Table 2).

Components 1 and 2 represent the same magnetic minerals with different grain sizes (Table 2). The former is SP Mgt (Mgh) just above the SP/SD threshold (~20–25 nm), which displays SD behavior as the measurement time was less than the thermal relaxation time [*Heslop et al.*, 2004]. The latter is SD Mgt (Mgh), which accounts for the most of the SIRM (46%–76%).

Component 3 with a $B_{1/2}$ of 100 mT in the parent material (69% of the SIRM) is PSD low-titanium titanomagnetite (TM). The coercive force of ~100 nm sized Mgt increases from 25 to 50 mT with a 10% increase in Ti content [*Dunlop and Özdemir*, 1997], which can explain the high B_{cr} of PSD TM observed in this study. *Ouyang et al.* [2015] also identified a component with $B_{1/2}$ of 101 mT as titanium-poor TM in samples from the bottom of a weathered basalt profile in the same area. Moreover, the T_C of TM decreases as the concentration of Ti increases and drops to 565°C with a 10% increase in Ti content [*Dunlop and Özdemir*, 1997; *Jiang et al.*, 2016; *O'Reilly*, 1984].

Component 3 with a $B_{1/2}$ of ~200 mT in samples from the SMZ (CM-22.6, CM-23.0, and CM-23.5) is fine-grained pedogenic Hm (Table 2). *Ouyang et al.* [2015] suggested that a component with $B_{1/2}$ of ~200 mT was pedogenic Hm in a profile of weathered basalt. This component is also present in red clay [*Nie et al.*, 2014] and loess [*Hu et al.*, 2013] on the CLP.

The high coercivity ($B_{1/2}$ of 631–891 mT) component 4 is present in all samples, and it only contributes $<4\%$ of the SIRM to the samples from the SMZ and parent material (Table 2). Such a high coercivity can only be attributed to antiferromagnetic minerals (Hm or Gt). *Hu et al.* [2013] characterized the magnetic mineralogy in Luochuan loess combining chemical dissolution, DRS, and magnetic techniques and found that detrital Hm has a $B_{1/2}$ of ~1 T. Gt has an average B_{cr} of ~3.4 T and thus cannot reach saturation in a low field [*Peters*, 2003]. Therefore, the high coercivity component 4 is considered to be SD Hm.

3.3. Hysteresis Loops, Day Plot, and First-Order Reversal Curve Diagrams

The hysteresis loop and its four parameters (B_c, B_{cr}, M_s, and M_{rs}) are useful diagnostic tools to investigate the mineralogy and grain size of geological samples [*Dunlop and Özdemir*, 1997; *Roberts et al.*, 1995]. The hysteresis loop of CM-21.1 in Figure 4a is obviously wasp-waisted, indicating the coexistence of at least two magnetic mineral components with strongly contrasting coercivities [*Roberts et al.*, 1995]. The hysteresis loops of CM-22.6, CM-23.0, and CM-23.5 indicate small coercivities and imply the presence of a large amount of SP

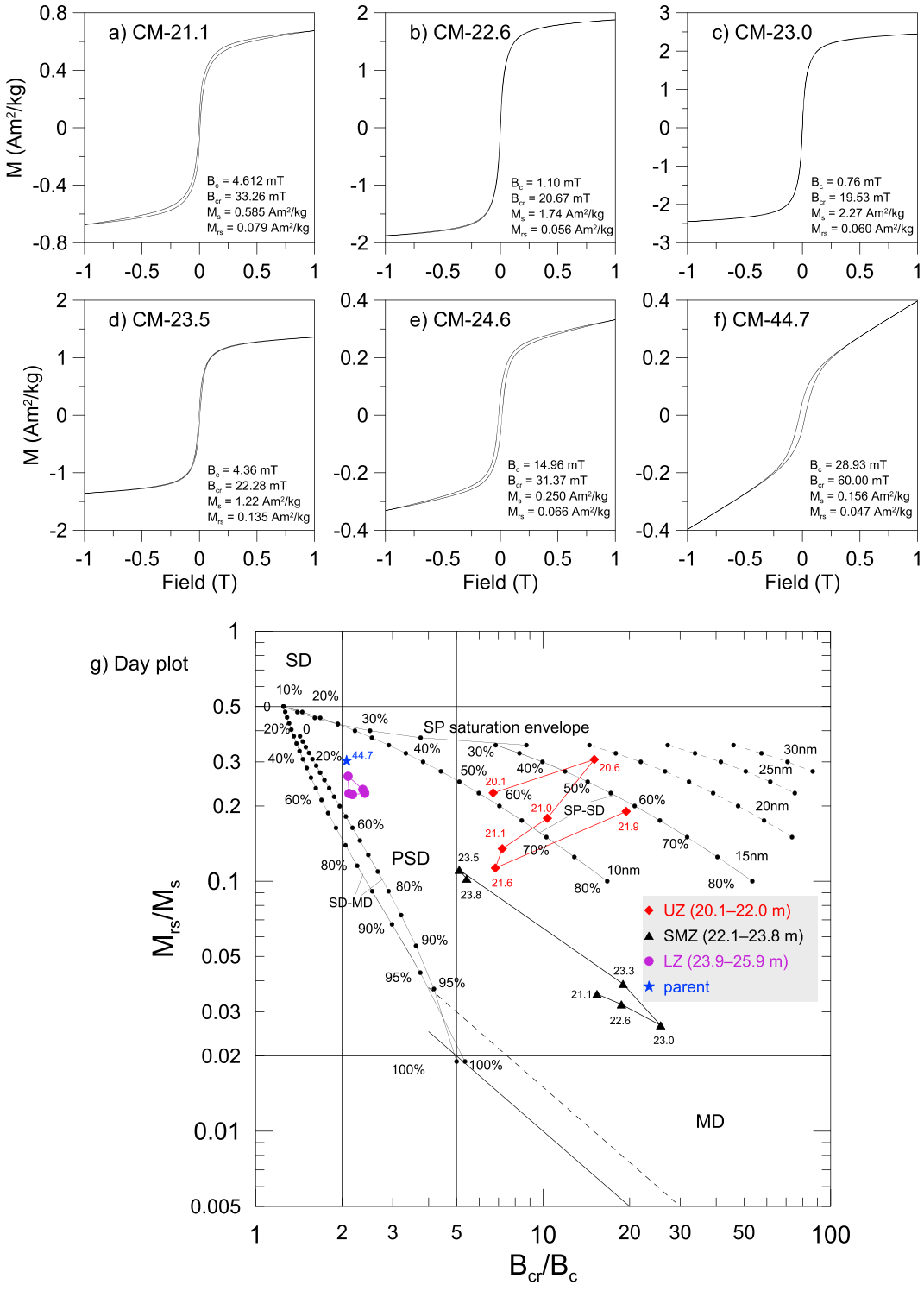

Figure 4. (a–f) Hysteresis loops for six selected samples. (g) Day plot for selected samples from 20.1 to 25.9 m depth (the background plot is from *Dunlop* [2002]). The red diamonds denote samples from the UZ (20.0–22.0 m). The black triangles denote samples from the SMZ (22.0–23.8 m). The purple circles are samples from the UZ (23.8–25.9 m). The blue star is the parent material (CM-44.7). The values annotated by symbols are sampling depths (e.g., 23.0 means that sample CM-23.0 was collected between 22.9 and 23.0 m depth).

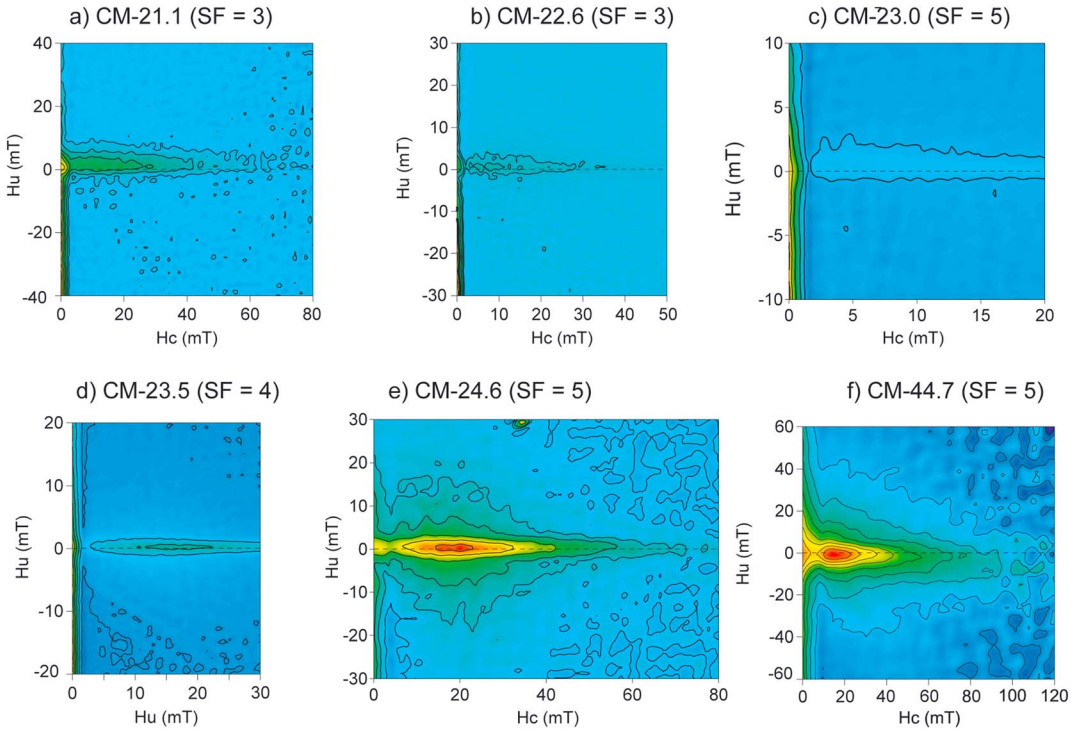

Figure 5. FORC diagrams for selected samples: (a) CM-21.1, $n = 150$, and field spacing (FS) = 1.1 mT; (b) CM-22.6, $n = 150$, and FS = 0.8 mT; (c) CM-23.0, $n = 120$, and FS = 0.4 mT; (d) CM-23.5, $n = 150$, and FS = 0.5 mT; (e) CM-24.6, $n = 150$, and FS = 1.0 mT; (f) CM-44.7, $n = 120$, and FS = 2.2 mT. All the smoothing factors (SFs) were estimated by FORCinel v1.18 [*Harrison and Feinberg*, 2008].

particles (Figures 4b–4d). The coercivities of CM-24.6 and CM-44.7 are much larger than those of the other samples, suggesting the presence of relatively "hard" minerals (Figures 4e and 4f).

Day plot shows the ratio of saturation remanence to saturation magnetization (M_{rs}/M_s) versus the ratio of coercivity of remanence to coercivity (B_{cr}/B_c), which is used to determine the domain state of geological samples dominated by Mgt and/or TM [*Day et al.*, 1977; *Dunlop*, 2002]. The Day plot for selected samples is displayed in Figure 4g. Samples in the SMZ (22.0–23.8 m) and UZ (20.0–22.0 m) are located in the SP + SD region, as defined by *Dunlop* [2002]. As illustrated in Figure 4g, the samples in the SMZ contain more SP particles than the other samples, particularly for samples at depths of about 23.0 m (>80%). In the SMZ, the concentration of SP particles first increases and then decreases with increasing depth. Among all the studied samples, CM-23.0 contains the most SP particles. Samples in the LZ (23.8–25.9 m), along with the parent material (CM44.7), plot in the PSD region, although close to the SD region.

FORC diagrams are a useful tool to identify the presence or absence of magnetostatic interactions and the contributions of SP, SD, PSD, and MD grains to the magnetization of a sample without the ambiguities of hysteresis data [*Pike et al.*, 1999; *Roberts et al.*, 2000, 2014]. FORC diagrams for selected samples are displayed in Figure 5. FORC diagrams for CM-23.0 ($M_{rs}/M_s = 0.03$; $B_{cr}/B_c = 25.6$) are shown in Figure 5c and display an obvious peak near the origin and a subtle elongate contour along the $H_u = 0$ axis, indicating the presence of noninteracting SD particles and dominant SP particles [*Roberts et al.*, 2000]. Samples CM21.1 ($M_{rs}/M_s = 0.31$; $B_{cr}/B_c = 15.1$), CM-22.6 ($M_{rs}/M_s = 0.03$; $B_{cr}/B_c = 18.7$), CM-23.5 ($M_{rs}/M_s = 0.11$; $B_{cr}/B_c = 5.1$), and CM-24.6 ($M_{rs}/M_s = 0.26$; $B_{cr}/B_c = 2.1$) have similar FORC diagrams as sample CM-23.0. There are peaks near the origin and secondary peaks centered on the $H_u = 0$ axis at ~10–20 mT, which have more obvious contours than those of CM-23.0, indicating that the relative concentration of noninteracting SD particles is high (Figures 5a, 5b, 5d, and 5e). In particular, CM-24.6 is dominated by SD particles with the clearest peaks centered at ~18 mT. The FORC diagrams for the parent material CM-44.7 ($M_{rs}/M_s = 0.3$; $B_{cr}/B_c = 2.07$) have two peaks that are centered near the origin and on the $H_u = 0$ axis at ~15 mT (Figure 5f). There are also asymmetric diverging contours that extend toward ~80–100 mT to the right of the diagrams, indicating the

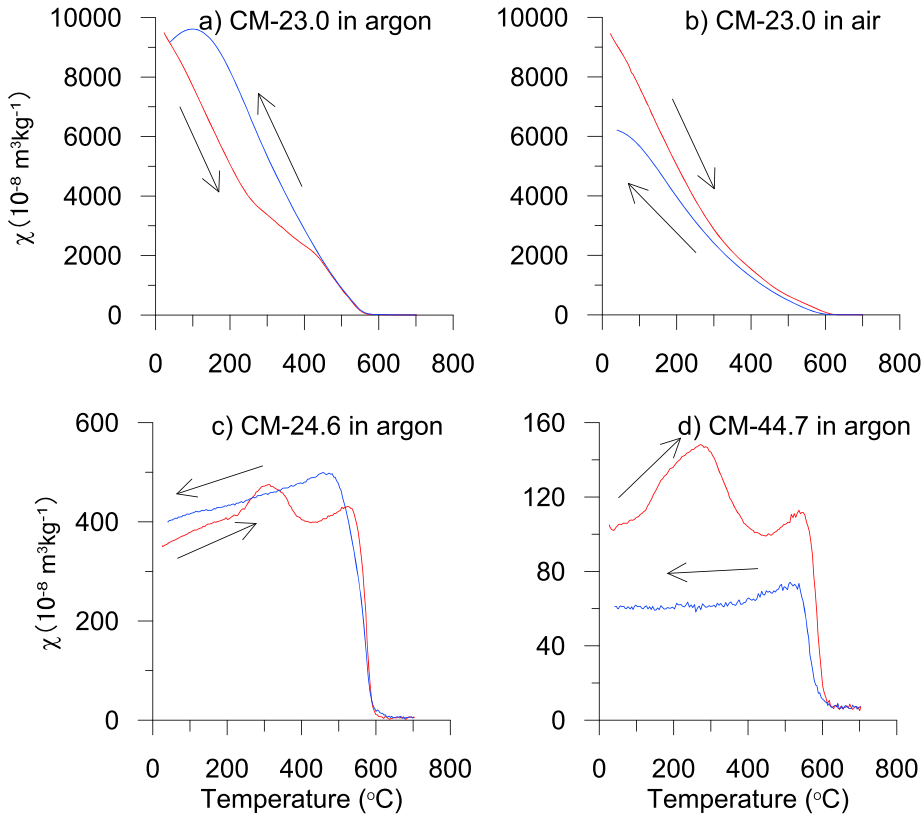

Figure 6. χ-*T* curves for typical samples: (a) CM-23.0 in argon, (b) CM-23.0 in air, (c) CM-24.6 in argon, and (d) CM-44.7 in argon.

presence of PSD particles. Therefore, the parent material (CM-44.7) contains SP, SD, and PSD particles [*Roberts et al.*, 2000, 2014].

3.4. High-Temperature χ-*T* Curves

χ-*T* curves for three typical samples (CM-23.0, CM-24.6, and CM-44.7) are shown in Figure 6. The χ-*T* curves of CM-23.0 were measured in both air and argon. All the heating curves drop sharply and the cooling curves increase abruptly at ~580°C, indicating the presence of Mgt. For sample CM-44.7, the Mgt is probably titanium-poor. Basalts from northern Hainan Island generally contain primary (titano-)magnetite [*Ho et al.*, 2000; *Ma et al.*, 2007; *Ouyang et al.*, 2015]. The T_C of TM decreases as the concentration of Ti increases and drops to 565°C with an increase in Ti content of 10% [*Dunlop and Özdemir*, 1997; *Jiang et al.*, 2016; *O'Reilly*, 1984].

In argon, the values of cooling curve for CM-23.0 are higher than those the heating curve, indicating the formation of strongly magnetic minerals during heating (Figure 6a). The cooling curve decreased from 120°C to room temperature due to the blocking of SP to SD particles that formed during heating [*Deng et al.*, 2000; *Liu et al.*, 2005b]. However, in air, the cooling curve for CM-23.0 is lower than the heating curve, suggesting the oxidation of Mgt and/or thermal conversion of Mgh to weakly magnetic Hm. Whether in air or argon, χ values of heating curves for CM-23.0 gradually decrease from room temperature to ~580°C, indicating the dominance of SP particles whose χ is inversely proportional to temperature ($\chi_{sp} = \mu_0 VM_s^2/3kT$, where μ_0 is the permeability of free space and *k* is Boltzmann's constant) [*Dunlop and Özdemir*, 1997].

For samples CM-24.6 and CM-44.7, the slight increase in χ from room temperature to about 280°C is attributed to the unblocking of SD magnetic particles [*Q. Liu et al.*, 2010; *Liu et al.*, 2005b], and the decrease from 280 to 450°C is due to the thermal conversion of strongly magnetic Mgh into weakly magnetic Hm [*Deng et al.*, 2000; *Liu et al.*, 2005b]. The values for the cooling curve of CM-24.6 are slightly higher than those of the

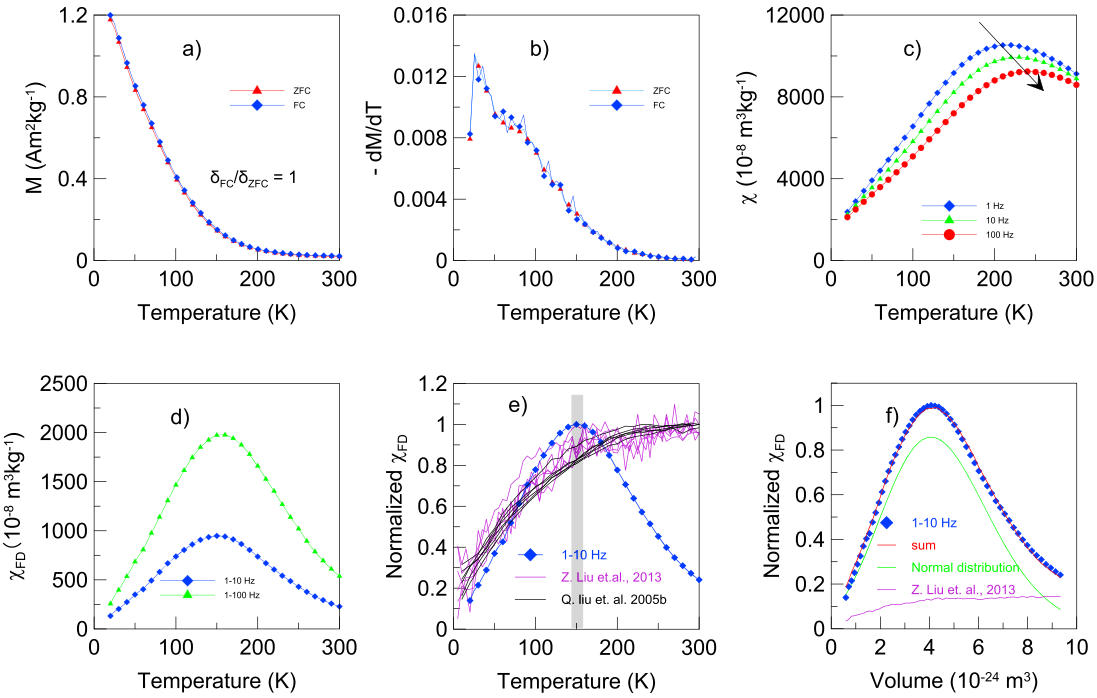

Figure 7. Low-temperature magnetic properties of CM-23.0: (a) zero-field cooling (ZFC) and field-cooling curves (FC); (b) first-order derivative curves (FORCs) of ZFC and FC; (c) low-temperature AC magnetic susceptibility at 1, 10, and 100 Hz; (d) low-temperature χ_{FD}-T (1–10 and 1–100 Hz); (e) normalized low-temperature χ_{FD}-T plot for CM-23.0, paleosol samples on the CLP [*Liu et al.*, 2005a], and B-horizon samples from modern soil profiles with MAP from 500 to 1300 mm/yr [*Liu et al.*, 2013]; and (f) normalized volume distribution of CM-23.0 unmixed into one GSD with a normal distribution of volume and the other GSD described by *Liu et al.* [2005a] and *Liu et al.* [2013].

heating curve, which can be attributed to the neoformation of ferrimagnetic minerals (e.g., Mgt) during the thermal treatment [*Deng et al.*, 2000; *Q. Liu et al.*, 2005b, 2010]. However, the χ values of the cooling curve for the parent material (CM-44.7) are lower than those of the heating curve, indicating that no or few new magnetic minerals formed and that at the same time, a considerable amount of strongly magnetic Mgh converted to Hm.

3.5. Low-Temperature ZFC/FC Curves and AC Susceptibility

Low-temperature SIRM warming curves for CM-23.0 after ZFC and FC treatment are displayed in Figure 7a. The ZFC and FC curves are almost identical. The remanence shows a rapid decrease below 150 K and then a more gradual decline to room temperature, due to the unblocking of SD into SP particles [*Q. Liu et al.*, 2012; *Moskowitz et al.*, 1993]. No Verwey transition is evident in the ZFC (or FC) curves and their derivative curves (Figures 7a and 7b). This is typical of superparamagnetism and consistent with the high χ_{FD} values for these samples (i.e., the presence of SP particles) [*Moskowitz et al.*, 1993]. δ_{FC}/δ_{ZFC} is used to identify biogenic magnetite (>2) [*Moskowitz et al.*, 1993], and a value of about 1 for CM-23.0 indicates that no biogenic magnetite is present.

Temperature-dependent magnetic susceptibility (χ) at 1, 10, and 100 Hz for sample CM-23.0 is shown in Figure 7c. χ values at 1, 10, and 100 Hz first increase and then decrease with increasing temperature. The temperatures that correspond to the maximum χ shift higher values with increasing frequency are at ~200, 220, and 240 K, respectively (Figure 7c). The low-temperature χ_{FD} variations (χ_{FD}-T curves) for sample CM-23.0 are shown in Figure 7d. χ_{FD} gradually increases with increasing temperature, and then decreases. χ_{FD} between 1 and 10 Hz and 1 and 100 Hz peak at ~150 K. The peak χ_{FD} value between 1 and 100 Hz is higher than that between 1 and 10 Hz, due to the wider range of grain size indicated by χ_{FD} (1–100 Hz). *Liu et al.* [2005a] proposed that the low-temperature χ_{FD}-T curve can be interpreted as an analog of the GSD of SP pedogenic particles and found that the dominant magnetic grain size of Chinese loess/paleosol samples lies just above the SP/SD boundary (~20–25 nm) with a fixed GSD. More importantly, the GSDs of fine-grained pedogenic

magnetic particles in loess/paleosols [*Liu et al.*, 2005a], red clay [*Nie et al.*, 2008], and modern soils [*Liu et al.*, 2013] are similar and independent of the degree of pedogenesis. However, the low-temperature χ_{FD}-*T* curve of sample CM-23.0 displays a different pattern with peaks at ~150 K, indicating a different origin for fine-grained pedogenic magnetic particles in the SMZ.

The low-temperature χ_{FD}-*T* curve (1 and 10 Hz) of sample CM-23.0 can be translated into an average grain size of ~19 nm for SP particles (Figures 7e and 7f) [*Liu et al.*, 2005a]. As shown in Figure 7f, the χ_{FD}-*T* curve for CM-23.0 has relatively high values in the right compared with the left and can be interpreted as the sum of SP particles with two different GSDs: one is a primary fraction of SP Mgt (Mgh) with an average grain size of ~19 nm and a normal distribution, and the other is a secondary fraction of pedogenic Mgt (Mgh) with a GSD similar to that described by *Liu et al.* [2005a].

3.6. Scatter Plots of Magnetic Parameters

In the UZ, χ correlates strongly with χ_{FD} (Figure 8a; $R^2 = 0.97$) but poorly with ARM and SIRM (Figures 8b and 8c; $R^2 = 0.11$ and 0.03, respectively). Similarly, in the SMZ, χ has a good correlation with χ_{FD} (Figure 8a; $R^2 = 0.65$) but poor negative correlations with ARM and SIRM (Figures 8b and 8c; $R^2 = 0.05$ and 0.16, respectively). However, in the LZ, χ displays significant correlations with χ_{FD}, ARM, and SIRM (Figures 8a–8c; $R^2 = 0.88$, 0.76, and 0.72, respectively). Therefore, χ enhancement in the UZ and SMZ is caused mainly by SP particles but in the LZ is attributed to both SP and SD particles.

χ_{FD} has a poor correlation with ARM in the UZ (Figure 8d; $R^2 = 0.18$). However, χ_{FD} correlates well with ARM in the LZ (Figure 8d; $R^2 = 0.85$), suggesting that the relative concentrations of SP and SD particles produced during pedogenesis are constant. The scatterplot of χ versus χ_{FD}/ARM can be used to evaluate the relative contribution of SP and SD particles to magnetic enhancement. χ_{FD}/χ_{ARM} ratios increase slightly (almost constant) with χ (~200–500 $\times 10^{-8}$ m^3 kg^{-1}) in the LZ but increase rapidly with χ (~500–2500 $\times 10^{-8}$ m^3 kg^{-1}) in the UZ (Figure 8e; $R^2 = 0.63$ and 0.85, respectively).

ARM correlates well with SIRM in the UZ, SMZ, and LZ (Figure 8f; $R^2 = 0.31$, 0.87, and 0.52, respectively). The ARM/SIRM best fit slope for the UZ (0.0153) has the highest value, indicating that it has the smallest grain size of magnetic particles above SP, followed by the SMZ (0.0116), and then the LZ (0.0067).

HIRM correlates negatively with the S-ratio in the UZ (Figure 8g; $R^2 = 0.82$), indicating the conversion of ferrimagnets (Mgt and Mgh) to Hm. As shown in Figures 8h and 8i, HIRM correlates negatively with χ_{FD} (ARM) in the UZ ($R^2 = 0.53$ and 0.19, respectively) but positively in the LZ ($R^2 = 0.41$ and 0.22, respectively). However, in the SMZ, there is no clear correlation between HIRM and χ_{FD} (Figure 8h; $R^2 = 0.05$), given that pedogenic SP particles only contribute a small part of the χ_{FD}, but SD magnetic particles mainly originate from pedogenesis, which thus results in a positive correlation between ARM and HIRM (Figure 8i; $R^2 = 0.23$).

3.7. Summary of Magnetic Properties

The magnetic minerals in the parent material are dominant SD Mgt (Mgh) and PSD titanium-poor TM, along with a small amount of SD Hm. The three studied zones are magnetically dominated by SP and SD Mgt (Mgh); in particular, the SMZ is controlled by SP Mgt (Mgh). There is no evidence for the existence of large magnetic particles (PSD and MD). Pedogenic fine-grained Hm is only present in the SMZ. SD Hm is present in the SMZ at extremely low concentrations but is present in the UZ at relatively high concentrations.

4. Discussion

4.1. Origin of the Magnetic Minerals

Under aerobic and free-draining conditions, the χ values of soil with initially weak magnetism are usually enhanced due to the presence of fine-grained ferrimagnetic particles. Possible mechanisms for this include (1) biogenic origins [*Fassbinder et al.*, 1990; *Lovley et al.*, 1987], (2) in situ and inorganic origins [*Maher and Taylor*, 1988; *Zhou et al.*, 1990], (3) wild fire [*Le Borgne*, 1960], and (4) fermentation [*Le Borgne*, 1955].

Biogenic Mgt generally involves two types of formation: extracellular formation of Mgt mediated by iron-reducing bacteria (GS-15) [*Lovley et al.*, 1987] and intracellular Mgt produced by microaerophilic assimilatory bacteria (magnetotactic bacteria; MTB) [*Fassbinder et al.*, 1990]. Mgt produced by iron-reducing bacteria requires strictly anaerobic conditions and has an uncontrolled GSD that is $<$50 nm. Mgt mediated by MTB

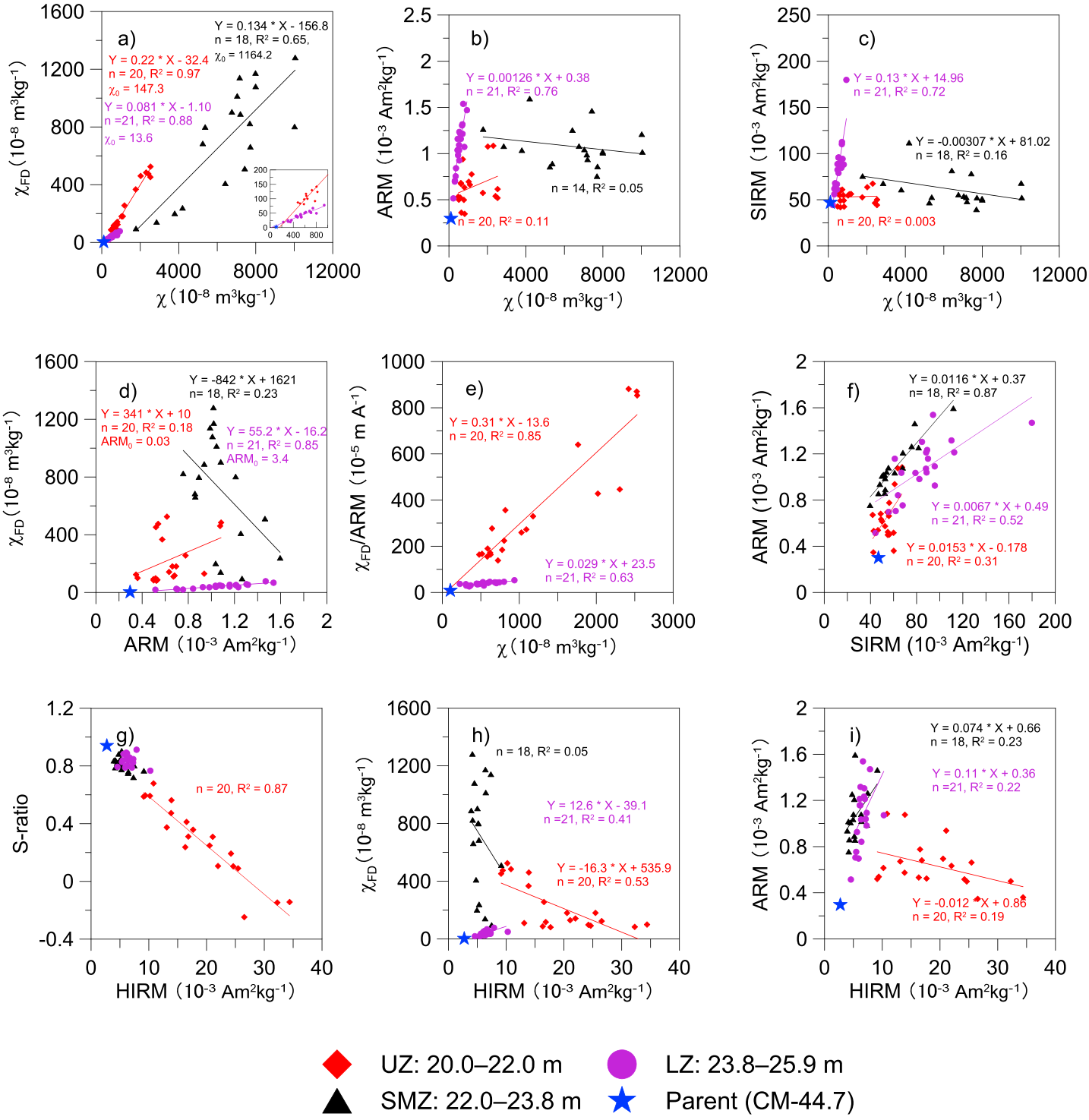

Figure 8. (a) χ versus χ_{FD} (X_0 is the x axis intercept); (b) χ versus ARM; (c) χ versus SIRM; (d) ARM versus χ_{FD}; (e) χ versus χ_{FD}/ARM; (f) ARM versus SIRM; (g) HIRM versus S-ratio; (h) HIRM versus χ_{FD}; (i) HIRM versus ARM. The text on each graph provides details of the correlations.

generally consists of chains of SD Mgt with diameters of 20–100 nm. *Liu et al.* [2005a] proposed that postformation dissolution of biogenic SD particles could result in a smaller size but cannot produce a fixed GSD. In the SMZ, the presence of Hm indicates aerobic conditions and that the magnetic enhancement is due to SP Mgt (Mgh) with fixed GSDs. More importantly, the low-temperature criteria δ_{FC}/δ_{ZFC} ratio is ~1,

which is inconsistent with the production of biogenic magnetite in our samples [*Moskowitz et al.*, 1993]. Thus, biogenic mechanisms cannot account for the magnetic enhancement in the SMZ.

Weakly magnetic minerals (Hm and hydroxides) can be converted to strongly magnetic Mgt (Mgh) by wild fire or crop burning in the presence of organic matter [*Le Borgne*, 1960]. It is believed that burning is insufficient to alter soil magnetism [*Dearing et al.*, 1996a]. Moreover, burning effects are generally restricted to the topsoil [*Thompson and Oldfield*, 1986] and do not affect the deeper soil horizons. Therefore, thermal transformation of weak magnetic minerals was not responsible for the magnetic enhancement of the SMZ.

Fermentation results in the anaerobic bacterial reduction of ferrihydrite to form SD Mgt (Mgh) with particle diameters of $<$100 nm [*Dearing et al.*, 1996a]. Organic matter can be a reductant for the formation of Mgt from other Fe(III) minerals, such as hematite [*Liu et al.*, 2005a]. Under inorganic conditions, in situ fine-grained Mgt could form by the oxidation of Fe(II) [*Maher and Taylor*, 1988]. *Dearing et al.* [1996a] combined the mechanisms of fermentation and in situ inorganic origins and proposed that ferrihydrite is formed in the presence of a strong Fe supply and reduced to Mgt, which may then be oxidized to Mgh. In other studies, magnetic enhancement has been attributed to Mgh formed from precursor ferrihydrite that was then transformed into hematite [*Barrón and Torrent*, 2002; *Michel et al.*, 2010; *Torrent et al.*, 2006]. Fine-grained Mgt (Mgh) that forms during pedogenesis is just above the SP/SD threshold with a fixed GSD and only accounts for a small fraction of the magnetic enhancement in the SMZ (Figure 7f).

Considering that the studied area is located in a volcanic belt, the major fraction of SP particles in sample CM-23.0 from the SMZ, which has a normal distribution of volume with an average grain size of ~ 19 nm (Figure 7f), is identified as volcanic ash. As illustrated in the FORC diagrams (Figure 5), the magnetic particles in the SMZ are noninteracting just as the volcanic samples reported by *Worm and Jackson* [1999] and *Till et al.* [2011]. *Worm and Jackson* [1999] demonstrated that the Yucca Mountain Tuff contains model SP TM grains of distinct sizes with a narrow GSD. The Yucca Mountain Tuff samples have an average grain size near the SP/SD threshold and have a χ_{FD}% of ~30%. But one sample with a small average grain size has a χ_{FD}% value of zero and an approximately normal volume distribution. The average grain size of SP magnetic particles in volcanic ash is determined by its cooling rate. *Till et al.* [2011] investigated the magnetic properties of samples from the Tiva Canyon Tuff and revealed that the grain size of magnetic particles changes progressively upward from SP near the base to PSD near the top of the sampled section. A possible reason for the relatively fine grain size of Mgh (Mgt) in the SMZ is that the air moisture around Hainan Island is high, which results in rapid cooling of the volcanic ash.

The present study area is located in northern Hainan Island in the Lei-Qiong area, which is a Quaternary volcanic belt in China. This belt includes $>$100 extinct volcanoes and ~7300 km^2 covering basalt [*Fan et al.*, 2004]. The eruptions in northern Hainan Island began in the early Eocene and were active in the Pleistocene. The final eruptions (Leihuling and Maanling) took place in the Holocene [*Fan et al.*, 2004]. The eruptions of the Lei-Qiong volcanoes were important geological events in southern China, but the exact timing of the volcanic events remains unclear, as primary minerals in the basalt have been largely altered by intense weathering. More than 20 different schemes of volcanic stages have been proposed for this belt [*Fan et al.*, 2004]. Magnetic identification of volcanic ash in the middle of the weathered basalt profile provides strong evidence that Quaternary basalts in northern Hainan Island were not formed by continuous eruptions.

4.2. Magnetic Enhancement and Paleoenvironmental Implications

The parent material of the studied soil may have had a variable composition due to its long weathering history and the possibility that it originated from a number of different volcanic eruptions. The analyzed samples from the three studied zones (UZ, SMZ, and LZ) have similar REE distributions, which implies a common geochemical origin (Figure 9). However, the primary minerals in the SMZ originated mainly from volcanic ash, resulting in the marked increase in χ and χ_{FD}. The UZ and LZ were formed from different volcanic eruption stages. χ_0 values (x axis intercept) from the χ-χ_{FD} plot for the UZ ($147.3\times10^{-8}\,m^3\,kg^{-1}$) are much higher than that for the LZ ($13.6\times10^{-8}\,m^3\,kg^{-1}$) (Figure 8a). However, the x axis intercept (ARM_0) in the scatterplot of ARM-χ_{FD} for the LZ ($3.4\times10^{-3}\,Am^2\,kg^{-1}$) is higher than that for the UZ (nearly zero) (Figure 8d). Therefore, the primary minerals in the LZ are mainly fine-grained SD particles with low χ, but in UZ, these are coarse-grained particles with high χ. As the grain size of magnetic minerals in basalt is related to the cooling rate

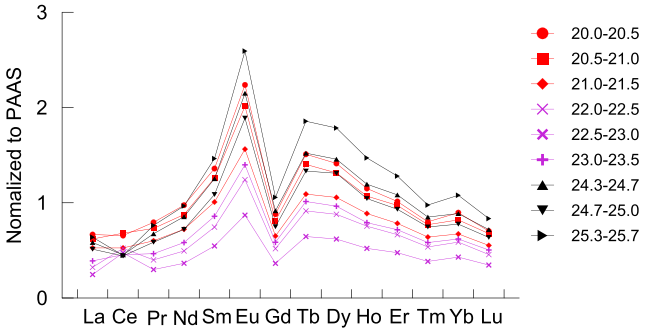

Figure 9. PAAS-normalized REE distributions for selected samples. The red color represents the UZ samples, the purple color denotes the SMZ samples, and the black color denotes the LZ samples. The blue line is for the parent material. PAAS refers to post-Archean Australian shale [*Nance and Taylor*, 1976].

of the lava [*Till et al.*, 2011; *Worm and Jackson*, 1999], the cooling rate for the unweathered basalt of the LZ was higher than that for the UZ.

As discussed above, the magnetic enhancement in the SMZ is attributed mainly to SP particles from volcanic ash. Magnetic enhancement in the UZ is due largely to the accumulation of SP particles during pedogenesis but in the LZ is attributed to both SP and SD particles. For the Quaternary loess/paleosol and underlying Pliocene red clay sequences on the CLP, magnetic enhancement is attributed to the accumulation of pedogenic SP and SD Mgt (Mgh), which has a fairly uniform GSD [*Liu et al.*, 2004, 2007; *Nie et al.*, 2007, 2008]. In the subtropical region (Zhejiang Province, eastern China), which has a MAP of 1100 mm/yr and MAT of 15.4°C, the Xiashu loess is also magnetically dominated by SD and SP Mgt (Mgh) and has a similar pedogenic environment to that of loess on the CLP [*Zhang et al.*, 2007]. However, *C. Liu et al.* [2012] investigated the magnetic properties of Xuancheng (MAP of 1400 mm/yr) and Qiliting (MAP of 1300 mm/yr) red soils in southeast China and found that vermiculated samples (χ of $\sim 20 \times 10^{-8}\,m^3\,kg^{-1}$) are low in fine-grained pedogenic Mgh and high in Hm, as compared with nonvermiculated samples. They further demonstrated that magnetic reduction of vermiculated samples was caused by iron dissolution and the transformation of highly magnetic Mgh to weakly magnetic Hm during a climate with high temperature and dry seasons combined with high precipitation.

Magnetic data for the parent material (blue star, CM-44.7) fall in the lower left parts of scatterplots except for the correlation between HIRM and S-ratio (Figure 8), indicating that new ferrimagnetic and antiferromagnetic minerals were formed during pedogenesis. However, the magnetic enhancement in the UZ and LZ differs from that of the loess/paleosol and red clay sequences discussed above. χ values are significantly enhanced in the UZ and LZ and much higher than those in loess and red clay. HIRM, proxy of Hm content, shows a similar pattern of variations as χ values. These results are attributed mainly to the parent basalt with a high iron content and the tropical climate with high precipitation (temperature). The degree of magnetic enhancement also differs between the UZ and LZ. The UZ contains more Hm and SP Mgt (Mgh) but less SD Mgt (Mgh) than the LZ (Table 1). As shown in Figures 8g–8i, pedogenic ferrimagnets (particularly SD Mgh) were transformed into Hm in the UZ. However, in the LZ, pedogenic SP and SD Mgh covaries with Hm (Figures 8h and 8i).

Parent material, topography, organisms, time, and climate are the five factors that determine soil properties [*Jenny*, 1941]. The parent material of the UZ and LZ has the same geochemical origin. The topography that formed both the UZ and LZ was subdued and flat. Organisms are generally associated with climate, and time is not an important factor in this study, as basalt is easily weathered, particularly in tropical regions. Therefore, climate is likely to be the dominant factor controlling the magnetic mineralogy of the UZ and LZ.

Dearing et al. [1996a] proposed that water activity and intense leaching influence the end-product of SFMs in soils on local scales. Our study area is located in a tropical region with a monsoonal climate. The wet seasons favor the formation of ferrihydrite that is the precursor to SP Mgh [*Barrón and Torrent*, 2002; *Cornell and Schwertmann*, 2003; *Dearing et al.*, 1996a]. The high temperature and seasonal drying favors the conversion of SD Mgh to Hm [*Cornell and Schwertmann*, 2003; *Torrent et al.*, 2006]. The UZ has a higher concentration of Hm and SP Mgt (Mgh) than the LZ, indicating that the former experienced higher precipitation and temperature than the latter.

A new pathway for Mgh formation has been proposed for magnetic enhancement in aerobic soils: ferrihydrite → SP maghemite → SD maghemite → hematite [*Barrón and Torrent*, 2002; *Michel et al.*, 2010; *Torrent et al.*, 2006]. This pathway links the paragenesis of Mgh and Hm in soil and is further supported by

the strong correlation between Hm content and χ_{FD}. The Hm/χ_{FD} ratio is controlled by climate and weathering intensity and tends to increase with decreasing rainfall in Russian steppe soils [*Torrent et al.*, 2006]. *Liu et al.* [2013] found that χ_{FD} and HIRM values (proxies of pedogenic Mgh and Hm, respectively) are linearly correlated in modern soil profiles. The best fit slope for χ_{FD}-HIRM first increases and then decreases with increasing MAP (threshold of ~1000 mm/yr). Mgh is formed faster than Hm when the MAP is under this threshold but is easily dissolved (altered) and/or converted to Hm when the MAP is higher than the threshold. *Cornell and Schwertmann* [2003] suggested that Hm is more difficult to dissolve and/or alter than Mgh in soil. As the MAP keeps increasing, the net production of Mgh decreases, whereas Hm gradually accumulates. Finally, when the MAP reaches a certain value, the net production of Mgh becomes negative and Hm will increase with decreasing Mgh. Notably, high temperatures favor the formation of Hm. Since the UZ experienced higher precipitation as well as temperature compared with the LZ during pedogenesis, HIRM negatively correlates with χ_{FD} (ARM) in the UZ but positively correlates with χ_{FD} (ARM) in the LZ (Figures 8h and 8i).

In the LZ, χ_{FD} is strongly correlated with ARM ($R^2 = 0.85$), suggesting that the relative concentration of SP and SD particles produced during pedogenesis was constant. A significant correlation between ARM and χ_{FD} commonly exists in loess/paleosol sequences on the CLP and modern soils formed under aerobic conditions with temperate MAP [*Q. Liu et al.*, 2012]. When the MAP is high, SFMs will be dissolved (altered) and/or converted into Hm, thereby causing the poor correlation between χ_{FD} and ARM in the UZ (Figure 8d). In the LZ, SP and SD particles have a similar formation rate with magnetic enhancement, whereas in the UZ, the production rate of SP particles is higher than that of SD particles (Figure 8e). *Long et al.* [2015] reported that χ_{FD}/χ_{ARM} ratios increase rapidly with low χ (~100–1000 $\times 10^{-8}$ $m^3 kg^{-1}$) but remain constant at high χ (~1000–3000 $\times 10^{-8}$ $m^3 kg^{-1}$) in red Ferralsols. However, the different formation rate between SP and SD particles is controlled mainly by water content, temperature, and Fe supply in the soil. The SP particles are formed from precursor ferrihydrite, and then slowly grow into SD particles [*Barrón and Torrent*, 2002; *Michel et al.*, 2010; *Torrent et al.*, 2006]. Ferrihydrite is metastable and is found mainly in soils that are wet but well drained with micropores [*Dearing et al.*, 1996a; *Torrent et al.*, 2006]. Aging experiments conducted on two-line phosphate ferrihydrite at 150 and 175°C revealed that the formation rate of SP Mgh is much higher than that of SD Mgh; the average grain size of aged samples is $<$20 nm in 90 of 120 days (150°C) or 12 of 14 h (175°C) [*Liu et al.*, 2008; *Michel et al.*, 2010]. When ferrihydrite is sufficiently abundant in soil with a relatively high water content (not saturated), the concentration of SP Mgh is much higher than that of SD Mgh, resulting in χ_{FD}/ARM showing a rapid increase with χ. Otherwise, χ_{FD}/ARM remains relatively constant and low with increasing χ (Figure 8e).

The conversion of relatively large SD Mgh particles to Hm in the UZ caused the remaining Mgh particles to become smaller. The ARM/SIRM best fit slope for the UZ is higher than that for the SMZ and LZ, indicating the smallest grain size of magnetic particles above the SP (Figure 8f). *Liu et al.* [2016] reported that the Sanmenxia loess generally has finer-grained pedogenic magnetic particles than the Luochuan loess because Sanmenxia is in the southeast of Luochuan and experienced higher precipitation and temperature. The reason for the humid and warm climate during the formation of the UZ remains unclear due to a lack of age data. Nevertheless, two possible mechanisms might be responsible for the humid and warm climate. One is that the climate changed from a glacial to interglacial period during the initial stage of UZ formation. The second is that the climate during the formation of the UZ was affected by CO_2 emitted by volcanic eruptions. Since the active volcanism occurred in the Lei-Qiong area during the Pleistocene, the continuous emission of CO_2 may have affected local climate by increasing temperature and precipitation. Further geochemical and paleomagnetic studies on this region may help to distinguish between these two possibilities.

5. Conclusions

Magnetic enhancement in the SMZ is attributed mainly to SP Mgt (Mgh) with two GSDs. The major fraction of SP particles originated from volcanic ash with an approximately normal volume distribution and average grain size of ~19 nm. The minor SP fraction is of pedogenic origin with a fixed GSD and average grain size just above the SP/SD threshold. The identification of volcanic ash in the red soil suggests that the Quaternary basalt in northern Hainan Island was not formed by continuous volcanic eruptions. The originally unweathered basalt of the UZ cooled more slowly and had a coarser magnetic grain size than that of the LZ. In addition, the magnetic enhancement of the UZ and LZ is attributed to the formation of SP and SD Mgt (Mgh)

during pedogenesis. The high concentration of Hm and SP Mgt (Mgh) in the UZ indicates that the UZ experienced higher precipitation and temperature than the LZ during pedogenesis.

Acknowledgments
All the data in this study can be obtained from the corresponding authors by e-mail. This study was supported by the National Natural Sciences Foundation of China (41325012). Zhifeng Liu was supported by the GIGCAS 135 Project (Y234091001) and the China Postdoctoral Science Foundation (2014M552245). Qingsong Liu further thanks supports from the National Key Research and Development Program of China (2016YFA0601903). Xing Ding was supported by the Strategic Priority Research Program of Chinese Academy of Science (XDB06030101). The authors thank X. Xu and Stallard Scientific Editing for improving the language of the manuscript. This is contribution IS-2360 from GIGCAS.

References

Balsam, W. L., B. B. Ellwood, J. Ji, E. R. Williams, X. Long, and A. El Hassani (2011), Magnetic susceptibility as a proxy for rainfall: Worldwide data from tropical and temperate climate, *Quat. Sci. Rev.*, *30*(19–20), 2732–2744, doi:10.1016/j.quascirev.2011.06.002.

Banerjee, S. K., J. W. King, and J. A. Marvin (1981), A rapid method for magnetic granulometry with applications to environmental studies, *Geophys. Res. Lett.*, *8*, 333–336, doi:10.1029/GL008i004p00333.

Barrón, V., and J. Torrent (2002), Evidence for a simple pathway to maghemite in Earth and Mars soils, *Geochim. Cosmochim. Acta*, *66*(15), 2801–2806.

Brimhall, G. H., L. Christopher, J. C. Ford, J. Bratt, G. Taylor, and O. Warin (1991), Quantitative geochemical approach to pedogenesis: Importance of parent material reduction, volumetric expansion, and eolian influx in lateritization, *Geoderma*, *51*(1), 51–91, doi:10.1016/0016-7061(91)90066-3.

Chesworth, W. (Ed.) (2008), *Encyclopedia of Soil Science*, Springer, Netherlands.

Chevrier, V., P. E. Mathé, P. Rochette, and H. P. Gunnlaugsson (2006), Magnetic study of an Antarctic weathering profile on basalt: Implications for recent weathering on Mars, *Earth Planet. Sci. Lett.*, *244*(3–4), 501–514, doi:10.1016/j.epsl.2006.02.033.

Cornell, R. M., and U. Schwertmann (2003), *The Iron Oxides, Structure, Properties, Reactions, Occurrences and Uses*, VCH, Weinheim, Germany.

Day, R., M. Fuller, and V. A. Schmidt (1977), Hysteresis properties of titanomagnetites: Grain-size and compositional dependence, *Phys. Earth Planet. Inter.*, *13*, 260–266.

Dearing, J. A., K. L. Hay, S. M. J. Baban, A. S. Huddleston, E. M. H. Wellington, and P. J. Loveland (1996a), Magnetic susceptibility of soil: An evaluation of conflicting theories using a national data set, *Geophys. J. Int.*, *127*(3), 728–734.

Dearing, J. A., R. J. L. Dann, K. Hay, J. A. Lees, P. J. Loveland, B. A. Maher, and K. O. Grady (1996b), Frequency dependent susceptibility measurements of environmental materials, *Geophys. J. Int.*, *124*, 228–240.

Deng, C. L., R. X. Zhu, K. L. Verosub, M. J. Singer, and B. Y. Yuan (2000), Paleoclimatic significance of the temperature-dependent susceptibility of Holocene loess along a NW-SE transect in the Chinese Loess Plateau, *Geophys. Res. Lett.*, *27*, 3715–3718, doi:10.1029/2000GL008462.

Dunlop, D. J. (2002), Theory and application of the day plot (M_{rs}/M_s versus H_{cr}/H_c). 2. Application to data for rocks, sediments, and soils, *J. Geophys. Res.*, *107*(B3), 2056, doi:10.1029/2001JB000486.

Dunlop, D. J., and Ö. Özdemir (1997), *Rock Magnetism: Fundamentals and Frontiers*, 573 pp., Cambridge Univ. Press, Cambridge, U. K.

Eggleton, R. A., C. Foudoulis, and D. Varkevisser (1987), Weathering of basalt—Changes in rock chemistry and mineralogy, *Clays Clay Miner.*, *35*(3), 161–169, doi:10.1346/Ccmn.1987.0350301.

Evans, M. E., and F. Heller (2003), *Environmental Magnetism: Principles and Applications of Environmagnetics*, 299 pp., Academic Press, Calif.

Eyre, J. K. (1997), Frequency dependence of magnetic susceptibility for populations of single-domain grains, *Geophys. J. Int.*, *129*(1), 209–211, doi:10.1111/j.1365-246X.1997.tb00951.x.

Fan, Q. C., Q. Sun, N. Li, and J. L. Sui (2004), Periods of volcanic activity and magma evolution of Holocene in north Hainan Island, *Acta Petrol. Sin*, *20*(3), 533–544.

Fassbinder, J. W. E., H. Stanjek, and H. Vali (1990), Occurrence of magnetic bacteria in soil, *Nature*, *343*, 161–163.

Florindo, F., R. Zhu, and B. Guo (1999a), Low-field susceptibility and palaeorainfall estimates. New data along a N-S transect of the Chinese Loess Plateau, *Phys. Chem. Earth Part A-Solid Earth Geodesy*, *24*(9), 817–821, doi:10.1016/s1464-1895(99)00120-9.

Florindo, F., R. X. Zhu, B. Guo, L. P. Yue, Y. X. Pan, and F. Speranza (1999b), Magnetic proxy climate results from the Duanjiapo loess section, southernmost extremity of the Chinese Loess Plateau, *J. Geophys. Res.*, *104*, 645–659, doi:10.1029/1998JB900001.

Han, J. M., H. Y. Lu, N. Q. Wu, and Z. T. Guo (1996), The magnetic susceptibility of modern soils in China and its use for paleoclimate reconstruction, *Stud. Geophys. Geod.*, *40*, 262–275.

Harrison, R. J., and J. M. Feinberg (2008), FORCinel: An improved algorithm for calculating first-order reversal curve distributions using locally weighted regression smoothing, *Geochem. Geophys. Geosyst.*, *9*, Q05016, doi:10.1029/2008GC001987.

Heslop, D., M. J. Dekkers, P. P. Kruiver, and I. H. M. van Oorschot (2002), Analysis of isothermal remanent magnetization acquisition curves using the expectation-maximization algorithm, *Geophys. J. Int.*, *148*(1), 58–64.

Heslop, D., G. McLntosh, and M. J. Dekkers (2004), Using time- and temperature-dependent Preisach models to investigate the limitations of modelling isothermal remanent magnetization acquisition curves with cumulative log Gaussian functions, *Geophys. J. Int.*, *157*(1), 55–63.

Ho, K., J. Chen, and W. Juang (2000), Geochronology and geochemistry of late Cenozoic basalts from the Leiqiong area, southern China, *J. Asian Earth Sci.*, *18*(3), 307–324, doi:10.1016/S1367-9120(99)00059-0.

Hu, P., Q. Liu, J. Torrent, V. Barrón, and C. Jin (2013), Characterizing and quantifying iron oxides in Chinese loess/paleosols: Implications for pedogenesis, *Earth Planet. Sci. Lett.*, *369-370*, 271–283, doi:10.1016/j.epsl.2013.03.033.

Huang, Z. G., W. Q. Zhang, J. H. Chen, R. H. Liu, and Z. C. He (1996), *Red Weathering Crust in South China (in Chinese)*, 312 pp., Ocean Press, Beijing.

Hyland, E. G., N. D. Sheldon, R. Van der Voo, C. Badgley, and A. Abrajevitch (2015), A new paleoprecipitation proxy based on soil magnetic properties: Implications for expanding paleoclimate reconstructions, *Geol. Soc. Am. Bull.*, *127*(7–8), 975–981, doi:10.1130/b31207.1.

Jenny, H. (1941), *Factors of Soil Formation: A System of Quantitative Pedology*, 281 pp., McGraw-Hill, New York.

Jiang, Z., Q. Liu, X. Zhao, A. P. Roberts, D. Heslop, V. Barrón, and J. Torrent (2016), Magnetism of Al-substituted magnetite reduced from Al-hematite, *J. Geophys. Res. Solid Earth*, *121*, 4195–4210, doi:10.1002/2016JB012863.

Jordanova, N., D. Jordanova, and P. Petrov (2016), Soil magnetic properties in Bulgaria at a national scale—Challenges and benefits, *Global Planet. Change*, *137*, 107–122, doi:10.1016/j.gloplacha.2015.12.015.

King, J. W., S. K. Banerjee, J. A. Marvin, and Ö. Özdemir (1982), A comparison of different magnetic methods for determining the relative grain size of magnetite in natural materials: Some results from lake sediments, *Earth Planet. Sci. Lett.*, *59*, 404–419.

Kruiver, P. P., M. J. Dekkers, and D. Heslop (2001), Quantification of magnetic coercivity components by the analysis of acquisition curves of isothermal remanent magnetisation, *Earth Planet. Sci. Lett.*, *189*(3), 269–276.

Le Borgne, E. (1955), Susceptibilité magnétique anormale du sol superficiel, *Ann. Geophys.*, *11*, 399–419.

Le Borgne, E. (1960), Influence du feu sur les propriétés magnétiques du sol et sur celles du schiste et du granite, *Ann. Geophys.*, *16*, 159–168.

Liu, C., C. Deng, Q. Liu, L. Zheng, W. Wang, X. Xu, S. Huang, and B. Yuan (2010), Mineral magnetism to probe into the nature of palaeomagnetic signals of subtropical red soil sequences in southern China, *Geophys. J. Int.*, *181*(3), 1395–1410, doi:10.1111/j.1365-246X.2010.04592.x.

Liu, C., C. Deng, and Q. Liu (2012), Mineral magnetic studies of the vermiculated red soils in southeast China and their paleoclimatic significance, *Palaeogeogr. Palaeoclimatol. Palaeoecol.*, *329–330*, 173–183, doi:10.1016/j.palaeo.2012.02.035.
Liu, Q., M. J. Jackson, S. K. Banerjee, B. A. Maher, C. Deng, Y. Pan, and R. Zhu (2004), Mechanism of the magnetic susceptibility enhancements of the Chinese loess, *J. Geophys. Res.*, *109*, B12107, doi:10.1029/2004JB003249.
Liu, Q., J. Torrent, B. A. Maher, Y. Yu, C. Deng, R. Zhu, and X. Zhao (2005a), Quantifying grain size distribution of pedogenic magnetic particles in Chinese loess and its significance for pedogenesis, *J. Geophys. Res.*, *110*, B11102, doi:10.1029/2005JB003726.
Liu, Q., C. Deng, Y. Yu, J. Torrent, M. J. Jackson, S. K. Banerjee, and R. Zhu (2005b), Temperature dependence of magnetic susceptibility in an argon environment: Implications for pedogenesis of Chinese loess/palaeosols, *Geophys. J. Int.*, *161*(1), 102–112, doi:10.1111/j.1365-246X.2005.02564.x.
Liu, Q., C. Deng, J. Torrent, and R. Zhu (2007), Review of recent developments in mineral magnetism of the Chinese loess, *Quat. Sci. Rev.*, *26*(3–4), 368–385, doi:10.1016/j.quascirev.2006.08.004.
Liu, Q., V. Barrón, J. Torrent, S. G. Eeckhout, and C. Deng (2008), Magnetism of intermediate hydromaghemite in the transformation of 2-line ferrihydrite into hematite and its paleoenvironmental implications, *J. Geophys. Res.*, *113*, B01103, doi:10.1029/2007JB005207.
Liu, Q., J. Torrent, H. Morrás, A. Hong, Z. Jiang, and Y. Su (2010), Superparamagnetism of two modern soils from the northeastern Pampean region, Argentina and its paleoclimatic indications, *Geophys. J. Int.*, *183*(2), 695–705, doi:10.1111/j.1365-246X.2010.04786.x.
Liu, Q., A. P. Roberts, J. C. Larrasoaña, S. K. Banerjee, Y. Guyodo, L. Tauxe, and F. Oldfield (2012), Environmental magnetism: Principles and applications, *Rev. Geophys.*, *50*, RG4002, doi:10.1029/2012RG000393.
Liu, T., and Z. Ding (1998), Chinese loess and the paleomonsoon, *Ann. Rev. Earth Planet. Sci.*, *26*(1), 111–145.
Liu, X., T. Rolph, J. Bloemendal, J. Shaw, and T. S. Liu (1995), Quantitative estimates of palaeoprecipitation at Xifeng in the loess plateau of China, *Palaeogeogr. Palaeoclimatol. Palaeoecol.*, *113*, 243–248.
Liu, Z., Q. Liu, J. Torrent, V. Barron, and P. Hu (2013), Testing the magnetic proxy chi(FD)/HIRM for quantifying paleoprecipitation in modern soil profiles from Shaanxi Province, China, *Global Planet. Change*, *110*, 368–378, doi:10.1016/j.gloplacha.2013.04.013.
Liu, Z., G. Wei, X. Wang, C. Jin, and Q. Liu (2016), Quantifying paleoprecipitation of the Luochuan and Sanmenxia loess on the Chinese Loess Plateau, *Palaeogeogr. Palaeoclimatol. Palaeoecol.*, *459*, 121–130, doi:10.1016/j.palaeo.2016.06.034.
Long, X., J. Ji, and W. Balsam (2011), Rainfall-dependent transformations of iron oxides in a tropical saprolite transect of Hainan Island, South China: Spectral and magnetic measurements, *J. Geophys. Res.*, *116*, F03015, doi:10.1029/2010JF001712.
Long, X., J. Ji, W. Balsam, V. Barrón, and J. Torrent (2015), Grain growth and transformation of pedogenic magnetic particles in red Ferralsols, *Geophys. Res. Lett.*, *42*, 5762–5770, doi:10.1002/2015GL064678.
Lovley, D. R., J. F. Stolz, G. L. Nord Jr., and E. J. P. Phillips (1987), Anaerobic production of magnetite by a dissimilatory iron-reducing microorganism, *Nature*, *330*, 252–254.
Ma, J., G. Wei, Y. Xu, W. Long, and W. Sun (2007), Mobilization and re-distribution of major and trace elements during extreme weathering of basalt in Hainan Island, South China, *Geochim. Cosmochim. Acta*, *71*(13), 3223–3237, doi:10.1016/j.gca.2007.03.035.
Maher, B. A. (1998), Magnetic properties of modern soils and Quaternary loessic paleosols: Paleoclimatic implications, *Palaeogeogr. Palaeoclimatol. Palaeoecol.*, *137*(1–2), 25–54.
Maher, B. A., and R. M. Taylor (1988), Formation of ultrafine-grained magnetite in soils, *Nature*, *336*, 368–371.
Maher, B. A., and R. Thompson (1995), Paleorainfall reconstructions from pedogenic magnetic susceptibility variations in the Chinese loess and paleosols, *Quat. Res.*, *44*(3), 383–391.
Maher, B. A., and R. Thompson (1999), *Quaternary Climates, Environments and Magnetism*, 390 pp., Cambridge Univ. Press, Cambridge, U. K.
Maher, B. A., R. Thompson, and L. P. Zhou (1994), Spatial and temporal reconstructions of changes in the Asian palaeomonsoon: A new mineral magnetic approach, *Earth Planet. Sci. Lett.*, *125*, 461–471.
Michel, F. M., V. Barron, J. Torrent, M. P. Morales, C. J. Serna, J. F. Boily, Q. Liu, A. Ambrosini, A. C. Cismasu, and G. E. Brown (2010), Ordered ferrimagnetic form of ferrihydrite reveals links among structure, composition, and magnetism, *Proc. Natl. Acad. Sci. U.S.A.*, *107*(7), 2787–2792, doi:10.1073/pnas.0910170107.
Moskowitz, B. M., R. Frankel, and D. Bazylinski (1993), Rock magnetic criteria for the detection of biogenic magnetite, *Earth Planet. Sci. Lett.*, *120*, 283–300.
Nance, W. B., and S. R. Taylor (1976), Rare-earth element patterns and crustal evolution: 1. Australian post-Archean sedimentary rocks, *Geochim. Cosmochim. Acta*, *40*(12), 1539–1551, doi:10.1016/0016-7037(76)90093-4.
Nie, J., J. W. King, and X. Fang (2007), Enhancement mechanisms of magnetic susceptibility in the Chinese red-clay sequence, *Geophys. Res. Lett.*, *34*, L19705, doi:10.1029/2007GL031430.
Nie, J., J. King, M. Jackson, X. Fang, and Y. Song (2008), AC magnetic susceptibility studies of Chinese red clay sediments between 4.8 and 4.1 Ma: Paleoceanographic and paleoclimatic implications, *J. Geophys. Res.*, *113*, B10106, doi:10.1029/2008JB005654.
Nie, J., R. Zhang, C. Necula, D. Heslop, Q. Liu, L. Gong, and S. Banerjee (2014), Late Miocene-early Pleistocene paleoclimate history of the Chinese Loess Plateau revealed by remanence unmixing, *Geophys. Res. Lett.*, *41*, 2163–2168, doi:10.1002/2014GL059379.
O'Reilly, W. (1984), *Rock and Mineral Magnetism*, 230 pp., Blackie & Son, Glasgow, Scotland.
Ouyang, T. P., Z. H. Tang, X. Zhao, C. J. Tian, J. L. Ma, G. J. Wei, N. S. Huang, M. K. Li, and Y. Bian (2015), Magnetic mineralogy of a weathered tropical basalt, Hainan Island, South China, *Phys. Earth Planet. Inter.*, *240*, 105–113, doi:10.1016/j.pepi.2015.01.001.
Peters, C. (2003), Selected room temperature magnetic parameters as a function of mineralogy, concentration and grain size, *Phys. Chem. Earth, Parts A/B/C*, *28*(16–19), 659–667, doi:10.1016/s1474-7065(03)00120-7.
Pike, C. R., A. P. Roberts, and K. L. Verosub (1999), Characterizing interactions in fine magnetic particle systems using first order reversal curves, *J. Appl. Phys.*, *85*(9), 6660–6667, doi:10.1063/1.370176.
Roberts, A. P., Y. L. Cui, and K. L. Verosub (1995), Wasp-waisted hysteresis loops: Mineral magnetic characteristics and discrimination of components in mixed magnetic systems, *J. Geophys. Res.*, *100*, 17,909–17,924, doi:10.1029/95JB00672.
Roberts, A. P., C. R. Pike, and K. L. Verosub (2000), First-order reversal curve diagrams: A new tool for characterizing the magnetic properties of natural samples, *J. Geophys. Res.*, *105*, 28,461–28,475, doi:10.1029/2000JB900326.
Roberts, A. P., D. Heslop, X. Zhao, and C. R. Pike (2014), Understanding fine magnetic particle systems through use of first-order reversal curve (FORC) diagrams, *Rev. Geophys.*, *52*, 557–602, doi:10.1002/2014RG000462.
Robertson, D. J., and D. E. France (1994), Discrimination of remanence-carrying minerals in mixtures, using isothermal remanent magnetization acquisition curves, *Phys. Earth Planet. Inter.*, *82*, 223–234.
Su, N., S.-Y. Yang, X.-D. Wang, L. Bi, and C.-F. Yang (2015), Magnetic parameters indicate the intensity of chemical weathering developed on igneous rocks in China, *Catena*, *133*, 328–341, doi:10.1016/j.catena.2015.06.003.
Thompson, R., and F. Oldfield (1986), *Environmental Magnetism*, 227 pp., Allen and Unwin, London, U. K.

Till, J. L., M. J. Jackson, J. G. Rosenbaum, and P. Solheid (2011), Magnetic properties in an ash flow tuff with continuous grain size variation: A natural reference for magnetic particle granulometry, *Geochem. Geophys. Geosyst.*, *12*, Q07Z26, doi:10.1029/2011GC003648.

Torrent, J., V. Barrón, and Q. Liu (2006), Magnetic enhancement is linked to and precedes hematite formation in aerobic soil, *Geophys. Res. Lett.*, *33*, L02401, doi:10.1029/2005GL024818.

Van Dam, R. L., J. B. J. Harrison, D. A. Hirschfeld, T. M. Meglich, Y. Li, and R. E. North (2008), Mineralogy and magnetic properties of basaltic substrate soils: Kaho'olawe and Big Island, Hawaii, *Soil Sci. Soc. Am. J.*, *72*(1), 244–257.

Worm, H. U. (1998), On the superparamagnetic-stable single domain transition for magnetite, and frequency dependence of susceptibility, *Geophys. J. Int.*, *133*, 201–206.

Worm, H. U., and M. Jackson (1999), The superparamagnetism of Yucca Mountain tuff, *J. Geophys. Res.*, *104*, 25,415–25,425, doi:10.1029/1999JB900285.

Zhang, W., L. Yu, M. Lu, X. Zheng, and Y. Shi (2007), Magnetic properties and geochemistry of the Xiashu loess in the present subtropical area of China, and their implications for pedogenic intensity, *Earth Planet. Sci. Lett.*, *260*(1–2), 86–97, doi:10.1016/j.epsl.2007.05.018.

Zhang, W., L. Yu, M. Lu, X. Zheng, J. Ji, L. Zhou, and X. Wang (2009), East Asian summer monsoon intensity inferred from iron oxide mineralogy in the Xiashu loess in southern China, *Quat. Sci. Rev.*, *28*(3–4), 345–353, doi:10.1016/j.quascirev.2008.10.002.

Zhou, L. P., F. Oldfield, A. G. Wintle, S. G. Robinson, and J. T. Wang (1990), Partly pedogenic origin of magnetic variations in Chinese loess, *Nature*, *346*, 737–739.